

Deformable Linear Object Surface Placement Using Elastica Planning and Local Shape Control

I. Grinberg¹ and A. Levin² and E. D. Rimon

Abstract—Manipulation of deformable linear objects (DLOs) in constrained environments is a challenging task. This paper describes a two-layered approach for placing DLOs on a flat surface using a single robot hand. The high-level layer is a novel DLO surface placement method based on Euler’s elastica solutions. During this process one DLO endpoint is manipulated by the robot gripper while a variable interior point of the DLO serves as the start point of the portion aligned with the placement surface. The low-level layer forms a pipeline controller. The controller estimates the DLO current shape using a Residual Neural Network (ResNet) and uses low-level feedback to ensure task execution in the presence of modeling and placement errors. The resulting DLO placement approach can recover from states where the high-level manipulation planner has failed as required by practical robot manipulation systems. The DLO placement approach is demonstrated with simulations and experiments that use silicon mock-up objects prepared for fresh food applications.

I. INTRODUCTION

This paper considers robotic manipulation of deformable linear objects, called DLOs. In these problems, one or two robot hands apply endpoint forces and torques that together with external influences such as gravity and environmental constraints affect the DLO shape during manipulation. This paper is motivated by SoftEnable project [1] where DLOs are used to model strip like fresh food items (Fig. 1). Other robotic applications include parts assembly [10], rope routing and untangling [2], [3] surgical suturing [4] and agricultural robotics [5]. DARPA’s Plug-Task [6], EU IntelliMan [7] and SoftEnable [1] and ICRA workshops [8]–[10] are all dedicated to soft and deformable object handling.

In previous work [11], we described a dual arm DLO steering scheme in the presence of obstacles. By exploiting Euler’s elastica solutions for DLO equilibrium shapes in two-dimensions, [11] plans DLO steering paths in two-dimensions and in semi-spatial manner in three-dimensions. However, the DLO was not allowed to contact features of the environment as such contacts apply reaction forces that affect the DLO shape. This paper considers manipulating DLOs by a single robot arm rather than dual arms. The single arm holds the DLO at one end while placing it on a tray or other flat surface in a stable non-self-intersecting and non-sliding manner (Fig. 1). Friction effects between the DLO and tray and between tray and table are also taken into account during placement. High-level planning of the robot hand movement uses the elastica shape parameters. A low-level controller uses a Residual Neural Network (ResNet) to ensure task

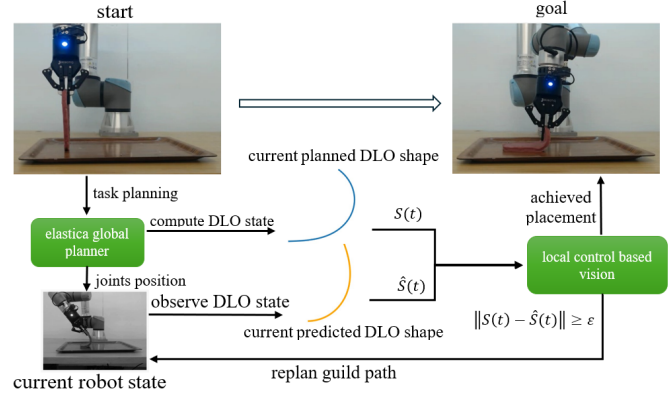


Fig. 1: A single robot arm has to place a strip-like fresh food item whose median axis is modeled as a DLO on a tray in a stable and non-self-intersecting manner. The DLO placement combines high-level planning with low-level feedback controller: $S(t)$ is the DLO high-level planned shape, $\hat{S}(t)$ is the ResNet measurement DLO observed shape. $\|S(t) - \hat{S}(t)\|$ is the DLO shape estimation error fed to the low-level controller.

execution in the presence of DLO modeling and placement errors (Fig. 1).

Related work: The equilibrium shapes of DLOs held under endpoint forces and moments in two-dimensions satisfy *Euler-Bernoulli’s bending law*, where the internal moment at each point is proportional to the DLO curvature at this point. See Wakamatsu [12] and Costanza [13] for surveys of DLO modeling techniques. In the robotics literature, sampling-based approaches are used to plan DLO steering paths [14]. Bretl [15] describes the DLO’s total elastic energy minimization as an optimal control problem, then uses the *adjoint equations* to design sample-based planners that steer flexible cables in 2-D and 3-D settings. Sintov [16] built upon this work by pre-computing DLO equilibrium shapes for sampled costates, then determining dual arm steering paths using numerical tests to avoid self-intersections and obstacles.

Local feedback control of DLO manipulation based on MPC schemes are described by Sintov [17], Yu [18] and Wang [19]. Navarro-Alarcon [20] and Lagneau [21] describe local shape control of DLOs using the *deformation Jacobian*, which relates changes in the DLO shape to the robot grippers velocity. This paper focuses on single arm manipulation using Euler’s elastica solutions for the DLO shapes [22]. The current paper extends Gu’s [23] vision based pipeline controller with a new *characterization* step, where ResNet uses vision measurements to compute the current DLO’s elastica parameters that are fed to the feedback controller.

Paper contributions: This paper proposes a two-layered approach for DLO placement on a flat surface of the environment. Each layer comes with its own novel contributions. The high-level layer divides the DLO placement into three

This work receives funding from European Union’s research and innovation program under grant agreement no. 101070600, project SoftEnable. Authors 1 and 2 made equal contributions. Dept. of ME, Technion, Israel.

stages: *free transport* that brings the DLO tip into contact with the surface, *tip rolling* against the surface then *full rolling placement* of the DLO under surface friction conditions. All stages are analytically characterized in terms of Euler's elastica solutions. The high-level planning of the robot gripper motion occurs in the space of elastica parameters defined for each placement stage. A key insight concerns the DLO curvature during placement. The DLO's bending moment (which is proportional to its curvature) varies continuously along its length. As a result, the DLO start point of the portion aligned with the surface has *zero curvature*. This insight allows the high-level planner to analytically compute the DLO's equilibrium shapes during placement.

The paper's low-level layer forms a pipeline controller consisting of two stages. The pipeline continuously estimates the flexible object's *medial axis* shape during placement. This medial axis forms the DLO model for the flexible object during placement. The DLO shape estimated in real time from an image taken by a camera, then cropped and converted into the DLO synthetic image using YOLOv8 [24]. The DLO's synthetic image is the input to the pipeline second stage. This stage estimates by direct regression the elastica parameters of the DLO current shape using ResNet50 [25]. The ResNet predicted elastica parameters are compared against the planned placement elastica parameters and fed into a local feedback controller which commands the robot hand (Fig. 1). Through simulations and comparative experiments, the paper demonstrates the effectiveness of this two-layered DLO placement method.

The paper is organized as follows. Section II summarizes Euler's elastica solutions for DLO equilibrium shapes. Section III describes the three-stage placement approach together with the elastica parameters that determine the DLO shape in each stage. Section IV describes the two-layered DLO placement scheme. Section V describes simulations statistics and experiments that compare semi-spatial placement of several mock-up fresh food items. Finally, Section VI summarizes the results and suggests future research topics.

II. DLO EQUILIBRIUM SHAPES IN FREE SPACE

This section reviews Euler's elastica solutions for DLO equilibrium shapes in two-dimensions. The DLO is modeled as a non-stretchable elastic rod of length L parameterized by arclength as $S(s) = (x(s), y(s), \phi(s))$ for $s \in [0, L]$. The DLO *state vector* consists of its x, y coordinates and tangent direction ϕ . The DLO curvature under arclength parametrization is given by $\kappa(s) = \frac{d}{ds}\phi(s)$. Using curvature as control input, $u(s) = \kappa(s)$, the DLO shape is described by the DLO *control system* [15]:

$$\frac{d}{ds}S(s) = \begin{pmatrix} \dot{x}(s) \\ \dot{y}(s) \\ \dot{\phi}(s) \end{pmatrix} = \begin{pmatrix} \cos \phi(s) \\ \sin \phi(s) \\ u(s) \end{pmatrix} \quad s \in [0, L]. \quad (1)$$

One can now use optimal control tools to minimize the DLO's total elastic energy

$$J = \frac{1}{2}EI \cdot \int_0^L u^2(s) ds$$

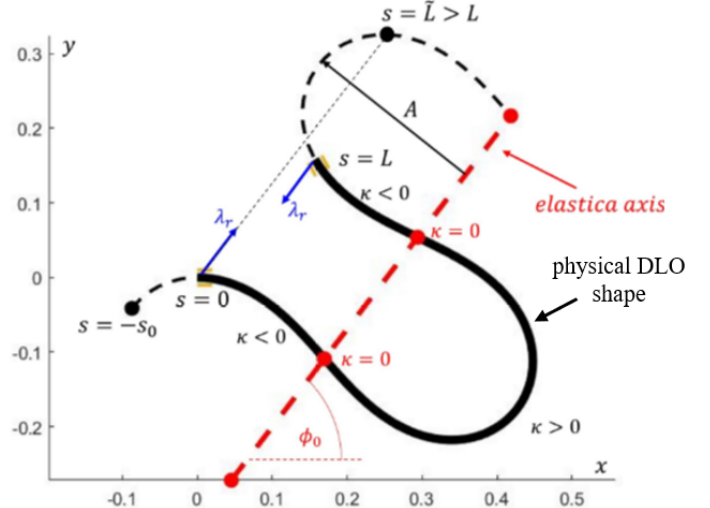


Fig. 2: Top view of full period elastica shape with the physical flexible cable of length L embedded in its periodic elastica solution of full-period length \bar{L} . The elastica axis with angle ϕ_0 passes through the zero curvature points and is parallel to the opposing forces of magnitude λ_r applied at cable endpoints.

under the DLO system constraints. Here $E > 0$ is Young's modulus of elasticity and $I > 0$ is the DLO cross-sectional second moment of inertia. The DLO *stiffness*, EI , is a known parameter. From calculus of variations, the *Hamiltonian* [26], [27] of the DLO system (1) is given by

$$H(S, \lambda, u) = \lambda_x \cdot \cos \phi + \lambda_y \cdot \sin \phi + \lambda_\phi \cdot u + \frac{1}{2}EI \cdot u^2$$

where $\lambda = (\lambda_x, \lambda_y, \lambda_\phi)$ are the *costate variables*. The costates correspond to internal force and bending moment along the DLO. The *adjoint equations* [28] determine the costate vector $\lambda(s)$ along energy extremal DLO shapes

$$\frac{d}{ds}\lambda(s) = -\frac{\partial}{\partial S}H(S, \lambda, u) \Rightarrow \begin{cases} \dot{\lambda}_x = 0 \\ \dot{\lambda}_y = 0 \\ \dot{\lambda}_\phi = \lambda_x \cdot \sin \phi(s) - \lambda_y \cdot \cos \phi(s) \end{cases} \quad (2)$$

Local minima shapes of the DLO's total elastic energy satisfy the additional condition

$$\frac{\partial}{\partial u}H(S, \lambda, u) = 0 \quad (3)$$

which leads to Euler Bernoulli bending law

$$\lambda_\phi(s) + EI \cdot u(s) = 0. \quad (4)$$

Using Eq. (2), $\lambda_x(s)$ and $\lambda_y(s)$ are constant along energy extremal DLO shapes. These constants define the parameter $\lambda_r = \sqrt{\lambda_x^2 + \lambda_y^2}$ which represents the magnitude of the opposing forces applied at the cable endpoints (blue arrows in Fig. 2), and the parameter ϕ_0 which defines the angle of the *elastica axis* that passes through the zero curvature points of the periodic elastica solution (red axis in Fig. 2).

Since the Hamiltonian of the DLO system has no explicit dependence on s , it remains constant along energy extremal DLO shapes, $H(s) = H^*$ for $s \in [0, L]$. Substituting $\lambda_\phi(s) = -EI \cdot u(s)$ from Eq. (4) into $H(s)$ and replacing $u(s)$ by $\kappa(s)$:

$$\lambda_r \cdot (\cos \phi(s) \cos \phi_0 + \sin \phi(s) \sin \phi_0) - \frac{1}{2}EI \cdot \kappa^2(s) = H^*. \quad (5)$$

Differentiating both sides w.r.t. s gives

$$\lambda_r \cdot (-\sin \phi(s) \cos \phi_0 + \cos \phi(s) \sin \phi_0) - EI \cdot \frac{d}{ds} \kappa(s) = 0 \quad (6)$$

where we canceled the common factor $\kappa(s) = \frac{d}{ds} \phi(s)$. Substituting the DLO system equations $\dot{x}(s) = \cos \phi(s)$ and $\dot{y}(s) = \sin \phi(s)$ into Eqs. (5)-(6) gives

$$\lambda_r \cdot R(\phi_0) \cdot \begin{pmatrix} \dot{x}(s) \\ \dot{y}(s) \end{pmatrix} = \begin{pmatrix} \frac{1}{2} EI \cdot \kappa^2(s) + H^* \\ EI \cdot \frac{d}{ds} \kappa(s) \end{pmatrix}$$

where $R(\phi_0) = \begin{bmatrix} \cos \phi_0 & \sin \phi_0 \\ \sin \phi_0 & -\cos \phi_0 \end{bmatrix}$. Integrating both sides, $\int_0^s \dot{x}(t) dt$ and $\int_0^s \dot{y}(t) dt$, gives the (x, y) coordinates of the DLO in terms of its curvature [29]:

$$\begin{pmatrix} x(s) \\ y(s) \end{pmatrix} = \begin{pmatrix} x(0) \\ y(0) \end{pmatrix} + \frac{1}{\lambda_r} R(\phi_0) \cdot \begin{pmatrix} \frac{1}{2} EI \cdot \int_0^s \kappa^2(\tau) d\tau + H^* \\ EI \cdot (\kappa(s) - \kappa(0)) \end{pmatrix} \quad (7)$$

where $s \in [0, L]$. Eq. (7) describes the DLO's equilibrium shapes in terms of the control input $u(s) = \kappa(s)$. This paper focuses on *inflectional elastica* [29] whose periodic solutions possess zero curvature (or inflectional) points (Fig. 2).

The DLO elastica shape parameters: The DLO equilibrium shapes can be described by three elastica parameters (Fig. 2). These are the elliptic modulus parameter, k , a phase parameter s_0 that measures the physical DLO start point, and the parameter \tilde{L} that measures the full period length of the underlying elastica solution (Fig. 2). The DLO equilibrium shapes in two-dimensions are thus determined by *six configuration parameters*: the DLO's base frame position and orientation, $(x(0), y(0), \phi(0))$, and the elastica parameters (k, s_0, \tilde{L}) .

III. DLO EQUILIBRIUM SHAPES IN CONTACT WITH A FLAT SURFACE OF THE ENVIRONMENT

This section describes a three-stage scheme for DLO placement on a planar surface of the environment. To begin with, it can be verified that gravity has only a negligible effect on DLO equilibrium shapes provided that their length remains reasonably short, roughly up to 50 cm for strip like fresh food items [11][Appendix B]. Hence, gravity is present but its minor effect is ignored here.

DLO shape in contact with a planar surface: Consider the placement constraint $C(s) = y(s) - y_0$, where y_0 is the height of the plane on which the DLO should be placed (Fig. 4). The elastic energy minimization problem now becomes

$$\begin{aligned} \min_u \quad & \frac{1}{2} EI \cdot \int_0^s u^2(\tau) d\tau \\ \text{s.t.} \quad & \frac{d}{ds} S(s) = (\cos \phi(s), \sin \phi(s), u(s)), \\ & \text{and } y \geq y_0. \end{aligned} \quad (8)$$

When the surface constraint is active, $C(s) = 0$, the equations

$$\begin{pmatrix} C(s) \\ \frac{d}{ds} C(s) \end{pmatrix} = \begin{pmatrix} 0 \\ 0 \end{pmatrix} \Rightarrow \begin{pmatrix} y(s) \\ \sin \phi(s) \end{pmatrix} = \begin{pmatrix} y_0 \\ 0 \end{pmatrix} \quad s \in [0, l]$$

where l is the length of the DLO segment that lies on the placement surface (Fig. 4(b)). The (x, y, ϕ) coordinates of the DLO surface contacting segment take the form

$$N(s) = \begin{cases} x(s) = x(0) + s \\ y(s) = y_0 \\ \phi(s) = 0 \text{ or } \pi \end{cases} \quad s \in [0, l]$$

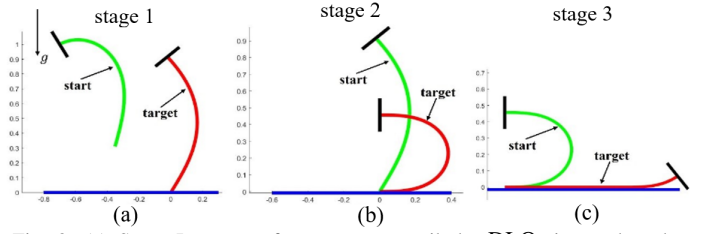


Fig. 3: (a) Stage I: contact free transport until the DLO tip touches the placement surface. (b) Stage II: non-slip rolling of the DLO tip against the surface until $\phi(0) = 0$. (c) Stage III: non-slip rolling placement of the entire DLO under surface friction conditions.

The *augmented Hamiltonian* [26], [27] under the surface placement constraint is given by

$$H(S, \lambda, u) = \begin{cases} \lambda \cdot \dot{S} + \frac{1}{2} EI \cdot u^2, & C(s) < 0 \\ \lambda \cdot \dot{S} + \lambda_\mu \cdot C(s) + \frac{1}{2} EI \cdot u^2 & C(s) \geq 0 \end{cases} \quad (9)$$

where $\lambda \in \mathbb{R}^3$ is the *costate vector* and $\lambda_\mu \leq 0$ is a Lagrange multiplier of the surface-contacting constraint.

Now consider the following observation concerning the DLO mechanics. Euler-Bernoulli's bending law (4) holds along the entire DLO length. The DLO's curvature is thus proportional to its bending moment along its entire length. The DLO curvature along its surface-contacting segment is identically zero. Since the bending moment $\lambda_\phi(s)$ varies *continuously* along the DLO entire length, the exit point from the surface-constrained segment at $s = l$ incurs zero bending moment and forms a *zero curvature* (or inflection) point.

In general, the elastica curvature equals to zero when $s + s_0 = \frac{\tilde{L}}{4}$ or $s + s_0 = \frac{3\tilde{L}}{4}$ (Fig. 2). The DLO shape during placement consists of two parts: a straight line from $s = 0$ to l aligned with the placement surface and the contact free portion from $s = l$ to L (Fig. 4(b)). The elastica parameter s_0 is set at the inflection point $\frac{\tilde{L}}{4}$ when the DLO has to be placed with *rightward* rolling (Fig. 4), and at the inflection point $\frac{3\tilde{L}}{4}$ when the DLO has to be placed with *leftward* rolling direction.

DLO placement three configuration spaces: Each of the DLO placement stages uses a different configuration space of parameters. In stage I the robot arm transports the DLO suspended vertically under the influence of gravity until its tip touches the placement surface (Fig. 3(a)). When stage I is performed in two-dimensions, the DLO is steered in the six-dimensional configuration space consisting of the *DLO* base frame position and orientation $(x(0), y(0), \phi(0))$ measured relative to the placement surface, then the contact free elastica parameters k, s_0, \tilde{L} . When Stage I is performed in a semi-spatial manner, the DLO is steered in the eight-dimensional configuration space consisting of the DLO base frame position and orientation $(x(0), y(0), z(0), \phi(0), \theta(0))$ where $\theta(0)$ is the base frame placement-plane rotation angle, then the contact free elastica parameters k, s_0, \tilde{L} . The configuration space of Stage I is thus $\mathcal{C}_1 = (x(0), y(0), \phi(0)) \times (k, s_0, \tilde{L}) \in \mathbb{R}^3 \times \mathbb{R}^3$ or $\mathcal{C}_1 = \{(x(0), y(0), z(0), \phi(0), \theta(0)) \times (k, s_0, \tilde{L}) \in \mathbb{R}^5 \times \mathbb{R}^3\}$.

In stage II the robot arm holds the DLO at its distal tip and executes non-slip rolling of the DLO's tip while maintaining point contact with the surface until the DLO tangent at the tip

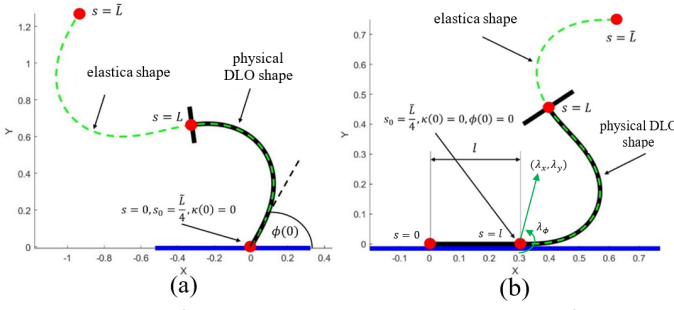


Fig. 4: (a) The DLO shape when the robot arm grasps the DLO at the red endpoint where $s = L$ while the DLO is supported by the surface at the tip where $s = 0$. When $s_0 = \frac{\tilde{L}}{4}$, the DLO rotates clockwise around the surface attachment point. (b) The DLO shape when the robot arm grasps the DLO at the red endpoint where $s = L$ with a surface-contacting segment of length l .

aligns with the surface at $\phi(0) = 0$ (Fig. 3(b)). In our practical setting the placement surface is a packing tray placed on a worktable. Hence, tip-tray as well as tray-table friction must be taken into account as discussed below. This paper assumes that the position of the DLO tip touching the surface is known. The DLO shape is characterized by *zero curvature* at the tip, as the contacting surface applies *zero bending moment* on the DLO. Since the DLO has zero curvature at the tip, the elastica parameter s_0 (the elastica solution start point) equals $\frac{\tilde{L}}{4}$ or $\frac{3\tilde{L}}{4}$. In stage II, three configuration parameters completely determine the DLO shape. This three-dimensional configuration space is defined as $C_2 = \{(\phi(0), k, \tilde{L}) \in \mathbb{R}^3\}$, where $\phi(0)$ is the tip tangent direction at the touch point, k is the elastica modulus parameter and \tilde{L} is the full-period length elastica parameter. Note that $(x(0), y(0))$ (or $(x(0), y(0), z(0), \theta(0))$ in 3-D) as well as s_0 remain *constant* under the tip's non-slip constraint (Fig. 4(a)).

In stage III the robot arm executes non-slip rolling of the DLO's contact free portion until it is fully placed on the surface (Fig. 3(c)). In this stage the robot gripper holds the DLO at one endpoint while a segment of length l touches the surface followed by a contact free elastica shape of length $L-l$ (Fig. 4(b)). In this stage, $s_0 = \frac{\tilde{L}}{4}$ or $s_0 = \frac{3\tilde{L}}{4}$ while the tip tangent is fixed at $\phi(0) = 0$. Hence, in stage III three configuration parameters completely define the DLO shape, with one parameter changed from stage II. This three-dimensional stage configuration space is defined as $C_3 = \{(l, k, \tilde{L}) \in \mathbb{R}^3\}$, where l is the variable length of the segment contacting the surface, k is the elastica modulus parameter and \tilde{L} is the full-period length elastica parameter.

Non-slip placement constraint: To prevent the DLO from slipping on the tray the tray from slipping on the table during placement, the DLO-tray and tray-table contact forces must lie inside their *Coulomb friction cone*. These two non-slip constraints are lumped into a single constraint using the coefficient of friction $\mu = \min\{\mu_1, \mu_2\}$, where μ_1 is the coefficient of friction between the DLO and the tray and μ_2 is the coefficient of friction between the tray and the table. The composite non-slip constraint is met when the DLO-tray contact force lies inside the friction cone defined by μ . Since the DLO curvature at the tip touching the surface is zero, the direction ϕ_0 of the tip contact force can be computed as a function of the elastica

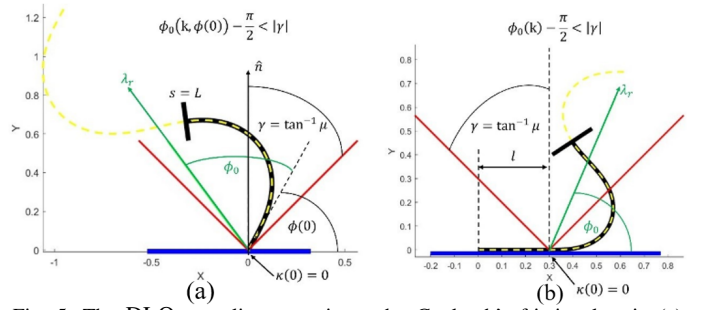


Fig. 5: The DLO non-slip constraint under Coulomb's friction law in (a) stage II, and (b) stage III of the three-stage placement scheme.

modulus parameter k [11]:

$$\phi_0 = \phi(0) \pm \tan^{-1}(1 - 2k^2) \quad (10)$$

where ϕ_0 is also the direction of the elastica axis (Fig. 5). When $s_0 = \frac{\tilde{L}}{4}$, a plus sign appears in Eq. (10). When $s_0 = \frac{3\tilde{L}}{4}$, a minus sign appears in Eq. (10). The friction cone constraint thus takes the form

$$\phi_0 - \alpha(\hat{n}) < |\tan^{-1}(\mu)| \quad \mu = \min\{\mu_1, \mu_2\}$$

where $\alpha(\hat{n})$ is the angle of the surface normal measured in the fixed world frame. For instance, $\alpha(\hat{n}) = \frac{\pi}{2}$ in Fig 5.

IV. LOCAL SHAPE CONTROL USING ELASTICA PARAMETERS AND MACHINE LEARNING

This section describes the DLO's local shape control pipeline (Fig. 1). Since the elastica parameters characterize the DLO shape, the control feedback computes a multi-valued *inverse function* from the DLO measured image to the elastica shape parameters. Verification of the elastica parameters along the planned trajectory can give the current state estimation of the system and transfer the DLO's observed shape to the controller. The controller can send a re-planning command that starts from the current state elastica parameters if the DLO's shape error exceeds a user-specified upper limit.

Controlled placement scheme: The DLO placement scheme planned a path. The algorithm utilized in this scheme can be found in our previous work [11], in this work the tray-contacting was added to the same scheme. Each node of the path is regarded as a ground truth. The low-level controller tries to minimize the *accuracy error* between the obtained DLO shape and the planned node. The accuracy error is the sum of the estimated shape error, the estimated elastica parameters error, and the estimated tangent error with different weights. The controller pipeline works using the following scheme: The input by the camera forms the current DLO shape frame, YOLOv8 crops the obtained frame from distractions, then extracts the DLO's medial axis [30] (skeleton of the object). The DLO's medial axis becomes the input to ResNet-50 network with three regression outputs, each one for a different elastica parameter. The output is the predicted elastica parameters. By knowing the predicted elastica parameters, the DLO shape is known. Since the inverse problem is *multi-valued*, ResNet is able to output several sets of candidate elastica parameters for the same measured DLO shape. Hence, the accuracy error between observed shapes determines if the real DLO shape is close to the planned shape.

The controller pipeline scheme is summarized as Algorithm 1. The algorithm accepts as input the DLO length L , the DLO base frame $(x(0), y(0), \phi(0))$, and the DLO observed image from the camera. The algorithm computes the accuracy error $\|S - \hat{S}\|$ and sends command to the robot arm according to the error value.

Algorithm 1 Vision Based Local Shape Control

Input: $x(0), y(0), \phi(0)$, DLO length L , DLO image frame

- 1: $cropped_image \leftarrow Crop(frame)$;
 - 2: $rotate_image \leftarrow rotate(cropped_image, \phi(0))$;
 - 3: $synthetical_image \leftarrow Skeleton(rotate_image)$;
 - 4: $(\bar{L}, k, s_0) \leftarrow Characterize(synthetical_image)$;
 - 5: $\hat{S} \leftarrow Get_shape(x(0), y(0), \phi(0), \bar{L}, k, s_0)$;
 - 6: **if** $\|S - \hat{S}\| \leq \varepsilon$ **then**
 - 7: $Continue$;
 - 8: **else**
 - 9: $Recovery$;
 - 10: **end if**
-

Dataset collection and generation: To train the proposed two ML models, multiple datasets were utilized. The first synthetic dataset was generated using iterative for-loops over the elastica parameters to capture their behavior. Each iteration step was determined based on the search step of the high-level planning algorithm (the iteration steps are detailed in the experiments section). This dataset aims to train the ResNet-50 learning model to predict the elastica parameters. The second synthetic dataset has the same purpose as the first dataset. However, the data underwent image processing to reduce noise and minimize interference in the ResNet-50 model learning process. The third dataset is an experimental one. This dataset aims to train the YOLOv8 model to leave the observed frame only with the DLO. The dataset was obtained through video recordings of DLOs using the laboratory camera (model specified in the experiments section), capturing frame-by-frame the obtained DLO shape. This multi-source dataset approach enabled comprehensive training of the controller pipeline across different scenarios.

Training and evaluation methodology: The controller pipeline training process was conducted in multiple stages: the initial stage was to train the ResNet-50 regression model to predict the elastica parameters using the first synthetic dataset. This stage tested three loss optimization functions, L1, MSE, and Huber, to optimize the ResNet-50 model predictions. The evaluation was performed on individual shapes using a structured dataset split into training, validation, and test sets. The accuracy metric $\|S - \hat{S}\|$, was checked for each epoch. Through this analysis, the identified error threshold required to achieve an accuracy level exceeding 90%. The results indicated that MSE and Huber loss functions provided the best performance (Fig. 6). The *Huber loss function* [31] takes the form

$$Loss_h = \begin{cases} 0.5(x_n - y_n)^2, & \text{if } |x_n - y_n| < \delta \\ \delta \cdot (|x_n - y_n| - 0.5 \cdot \delta) & \text{otherwise} \end{cases}$$

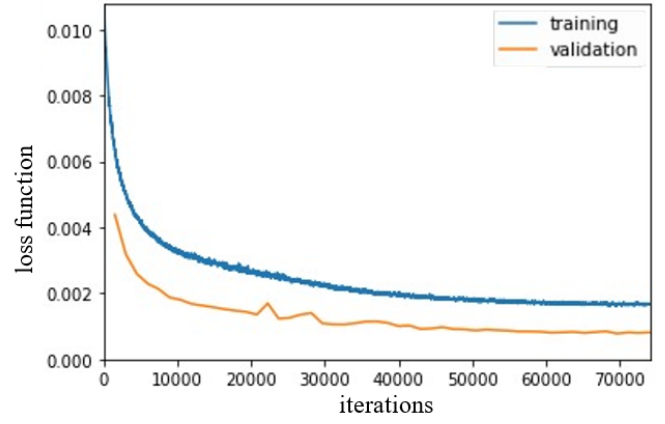


Fig. 6: The loss optimization process for the ResNet-50 model.

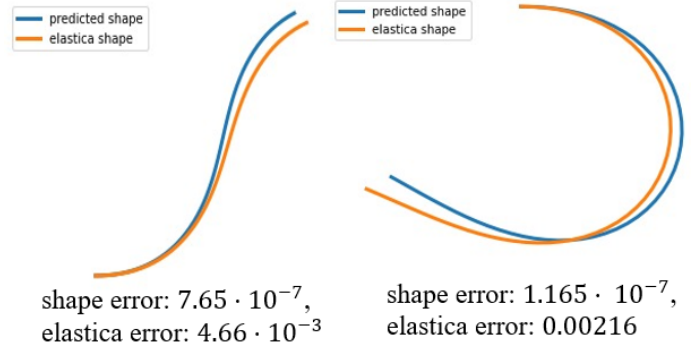


Fig. 7: Evaluation methods of ResNet-50 are the shape error and the elastica parameters error: comparison between the ground truth DLO (orange) and predicted DLO (blue). The shape error is the distance between each point $(x(s), y(s))$ for $s \in [0, L]$ on each line. The elastica error is the MSE metric between the $[\bar{L}, s_0, k]$ labels from the planer and the prediction from the ResNet-50 model. It can be inferred that the ResNet-50 model's prediction is good because the error is low.

where x_n is the vector of ground truth elastica parameters and y_n is the vector of predicted elastica parameters, δ is a numerical value that defines the boundary where Huber's loss function transitions from quadratic to linear. The second training stage was to try to optimize ResNet-50 prediction using the second dataset, which led to an improvement in the average accuracy error in the total trajectory. These two stages form the DLO *characterization model*. Examples comparing the DLO shape and elastica parameters errors from the test set are shown in Fig. 7.

During the final training stage YOLOv8 model was trained to crop the current observed DLO frame. Using the experimental dataset to generate focused, cropped images. The YOLOv8 model was trained on a minimal dataset and has done the DLO isolation. The cropped images were then passed to the controller pipeline for further refinement. The YOLOv8 model mask cannot be considered a characterization of the DLO shape because the cropped image has many inaccuracies, which the estimation of the elastica parameters corrects and guarantees the DLO shape.

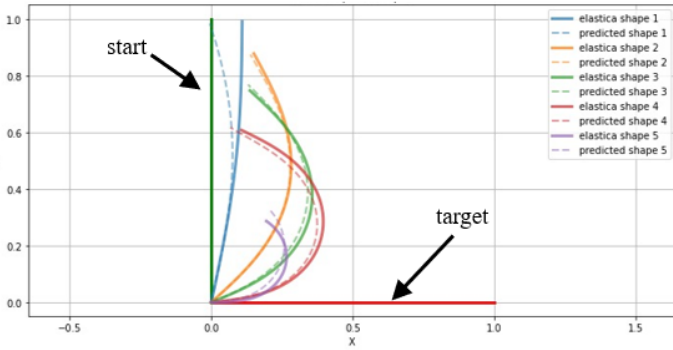


Fig. 8: Five DLO frames sampled during placement. The green vertical line is the DLO start position, the horizontal red line is the DLO target placement. The colors distinguish between each sampled frame. In each frame the bold curve is the elastica planned shape and the dashed curve is the ResNet predicted DLO shape. The surface attachment point is located at $(0, 0)$.

V. REPRESENTATIVE SIMULATIONS AND EXPERIMENTS

This section describes representative simulations followed by DLO placement experiments. The placement planning code will be posted at the Github [32].

Simulation results: The simulations are aimed at evaluating the low-level controller on synthetic DLO placement paths and to demonstrate the DLO placement scheme. The placement scheme was implemented in Python and run on DELL Precision 7865 with Ubuntu 22.04 desktop, AMD Threadripper PRO 5945WX Processor, 32GB RAM, 16GB GPU Quadro RTX a4000. The placement scheme received as input the base frame position $x(0), y(0), \phi$ and elastica parameters \tilde{L}, s_0, k of the DLO start and target positions. The resolution of the configuration parameters: $\Delta x(0) = \Delta y(0) = \Delta z(0) = 0.01 \cdot L$ [m], $\Delta \phi(0) = \Delta \theta = 2^\circ$, $\Delta \tilde{L} = 0.02L$, $\Delta k = 0.005$, $\Delta l = 0.05 \cdot L$, and $s_0 = \frac{\tilde{L}}{4}$. The sampling rate is 7 [fps]. The output is the observed DLO shape projection. This shape was inserted into the controller pipeline. The section describes three ranking methods of the controller performance: the shape error, the elastica parameters error, and the tangent error. The errors are between the observed DLO configuration and the planned configuration in each sample frame on the manipulation trajectory. The results are shown in Fig. 8. Five sampled frames simulated and obtained path are compared in Fig. 8. A multiple-path checking was made on 22 paths including 1015 shapes shown in Fig 9. Each box represents an error type distribution based on the mean and std. These distributions are used to determine the accuracy error threshold ε . The controller will send a re-planning message when the computed accuracy error exceeds this value. The shape error is 0.0020 ± 0.0061 [m], the elastica error is 0.4766 ± 0.6288 , and the tangent error is 0.1873 ± 0.8721 [rad]. All errors are shown by the mean \pm standard deviation. Because the problem of the elastica parameters is a multi-valued function, it can be seen that the elastica parameters mean error is close to the median (Fig. 9). That is why the elastica parameters have a low weight relative to the other errors.

Real world experiments: The proposed framework has been validated through experiments. Four silicon mock-up objects were prepared: steak, salmon, bass fillet and yellow

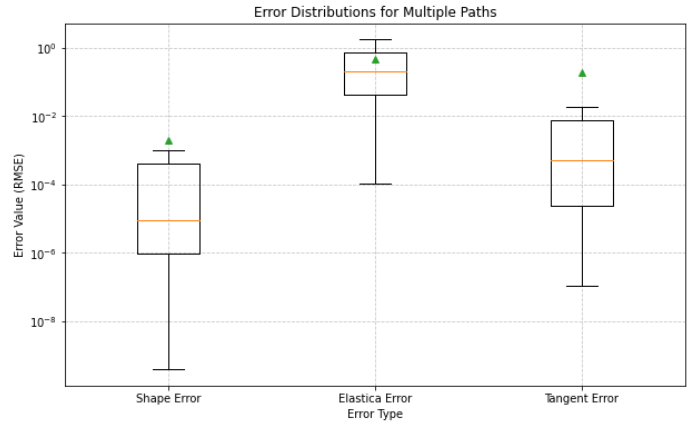


Fig. 9: The three error distributions: shape error, elastica error, and tangent error. The orange line is the median of each error, and the green triangle is the mean. It can be understood from the box-plot that more than 90% of the predicted shapes are good. It means the controller works well. The error value axis is in log scale.

cheese. The experiment setup is shown in Fig. 1. A UR5e robot arm with a Robotiq 2F-85 gripper performs the DLOs placement on a tray supported by a worktable. A Logi-1080HD web camera is utilized to observe the DLO shape. The camera is exposed to the profile of the DLO. The three verification methods proposed were: execution time, task success, and small accuracy error. A comparison was made between four different mock-up silicon objects. The task is to place the object comfortably on a tray without slipping or wrinkling, which can damage the DLO. In Fig. 10 for all cases the task was successful. The two-layered placement average execution time was 55 seconds with standard deviation of 5 seconds. There is a correlation between task execution time and object length L , with smaller objects taking less time to place. In that manner of the accuracy error, the shape error is 0.00752 ± 0.00306 [m], the elastica error is 0.1271 ± 0.0774 . Those errors in the steak and the salmon cases are better than the cheese and bass fillet objects (Fig. 11). The tangent error has a large mean and standard deviation. This can be explained as sensitivity of the tangent error to the DLO thickness. As the cheese and the bass fillet objects are thinner than the steak and salmon objects. The controller pipeline thus works better with the salmon and beef steak objects.

VI. CONCLUSION

The paper described a two-layered DLO surface placement approach. The high-level layer is a three-stage placement scheme based on Euler's elastica solutions. The low-level layer is a visual perception controller monitoring execution of the robot arm placement process. The high-level layer uses three stages to plan the DLO placement. First free transport in a six-dimensional configuration space (eight-dimensional in the case of semi-spatial placement), then two types of three-dimensional configuration spaces of the elastica parameters during DLO during tip rolling and full placement in contact with the planar surface. All placement stages are performed under non-slip conditions in a locally stable through local minima of the DLO's elastic energy and in non self-intersecting

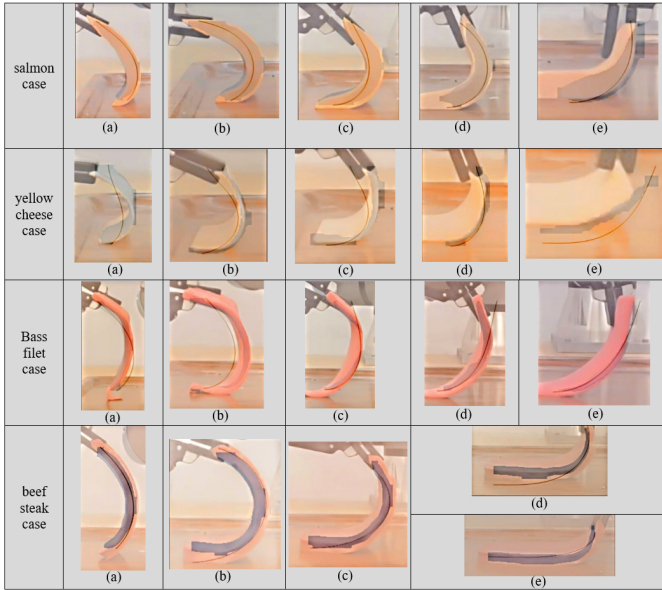


Fig. 10: (a)-(e) Four different cases of the two-layered DLO placement experiments. Each image shows a particular frame of the DLO placement process. Each image describes the three layers of the controller pipeline. The first layer (background) is the crop stage, the second layer (blue polygon) is the image synthetic stage, the third layer (black curve) shows the observed DLO shape computed by ResNet-50's predicted elastica parameters.

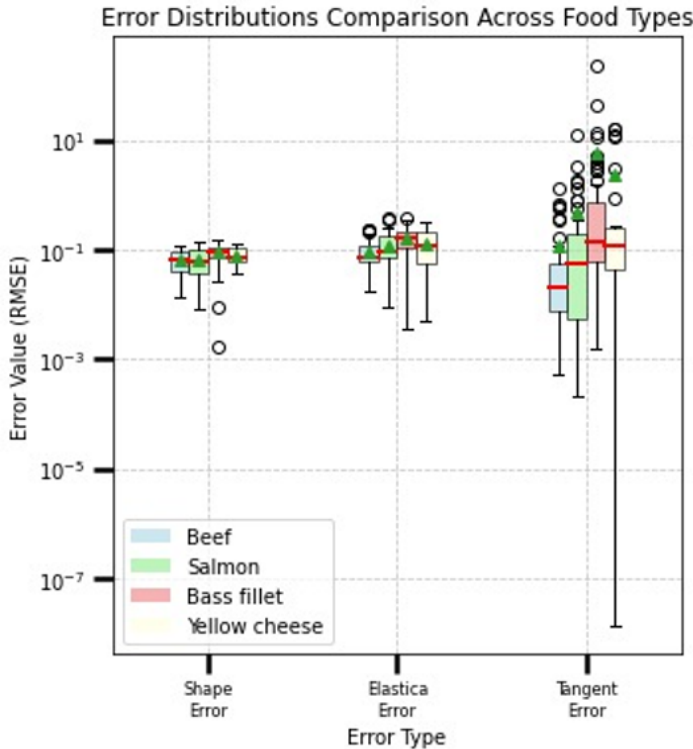


Fig. 11: Three error distributions in real use-cases. In the shape and elastica errors, the median (red lines) and mean (green triangle) error of observed shapes and the elastica parameters are similar and very close in the different cases. Thus indicates that there is no effect of the object type and it can be assumed that they are all DLOs. In contrast, the tangent error is influenced by the type of object thickness.

manner. Practical realization of the DLO planned placement path is monitored by a low-level perception controller that uses *ML* pipeline to estimate the accuracy error between the observed and planned DLO shapes during task execution in the presence of modeling and placement errors.

Future research will consider several topics. The high-level planner will be augmented by computation of the DLO equilibrium shapes under *elastic and gravitational* energies. This extension will require numerical solution of the DLO's adjoint equations rather than the closed form elastica solutions. In addition, the reverse process of this paper's placement scheme could be adapted for DLO pick-up from a surface such as a conveyor belt. At the low-level control, under this paper's method when the controller gets a high accuracy error, it sends a command of recovery and re-plans the DLO's placement path from the current observed state. By adding a *Kalman filter*, prediction of the DLO shape and position can be made before the manipulation starts. The controller will then be able to estimate the accuracy error and react before any physical movement of the robot arm begins. Finally, reinforcement and imitation learning techniques can learn a policy and rewards based on this paper's accuracy error, then improve on the ResNet elastica parameters computation used by this paper.

REFERENCES

- [1] "Softenable – towards soft fixture-based manipulation primitives enabling safe robotic manipulation in hazardous healthcare and food handling applications," European Union Horizon Project, <https://softenable.eu/>, 2022.
- [2] M. Mukadam, A. Borum, and T. Bretl, "Quasi-static manipulation of a planar elastic rod using multiple robotic grippers," in *IROS*, 2014, pp. 55–60.
- [3] V. Viswanath, K. Shivakumar, and J. K. et al., "Autonomously untangling long cables," in *Robotics: Science and Systems (RSS)*, 2022.
- [4] R. C. Jackson and M. C. Cavusoglu, "Needle path planning for autonomous robotic surgical suturing," in *ICRA*, 2013, pp. 1669–1675.
- [5] O. Aghajanzadeh, M. Aranda, J. A. C. Ramon, C. Cariou, R. Lenain, and Y. Mezouar, "Adaptive deformation control for elastic linear objects," *Frontiers in Robotics and AI*, vol. 9, pp. 1–13, Article 868459, 2022.
- [6] P. Chang and T. Padir, "Model-based manipulation of linear flexible objects: Task automation in simulation and real world," in *IEEE/ASME Int. Conf. on Advanced Intelligent Mechatronics*, 2020, pp. 6–10.
- [7] "Intelliman – AI-powered manipulation system for advanced robotic service, manufacturing and prosthetics," European Union Horizon Project, <https://intelliman-project.eu/>, 2022.
- [8] C. D. J. Zhu, A. Cherubini, D. Navarro, F. Alameghi, D. Berenson, F. Ficuciello, K. Harada, J. Kober, X. LI, J. Pan, W. Yuan, and M. Gienger, "Challenges and outlook in robotic manipulation of deformable objects," *IEEE Robotics & Automation Magazine*, pp. 2–12, 2022.
- [9] "3rd workshop on representing and manipulating deformable objects," ICRA, <https://deformable-workshop.github.io/icra2023/>, 2023.
- [10] "4th workshop on representing and manipulating deformable objects," ICRA, <https://deformable-workshop.github.io/icra2024/>, 2024.
- [11] A. Levin, I. Grinberg, E. D. Rimon, and A. Shapiro, "Dual arm steering of deformable linear objects in 2-D and 3-D environments using Euler's elastica solutions," *arXiv:2502.07509*, 2025.
- [12] H. Wakamatsu and S. Hirai, "Static modeling of linear object deformation based on differential geometry," *The Int. J. of Robotics Research*, vol. 23, no. 3, pp. 293–311, 2004.
- [13] C. Armanini, F. Boyer, A. T. Mathew, C. Duriez, and F. Renda, "Soft robots modeling: A structured overview," *IEEE Transactions on Robotics*, 2022.
- [14] M. Moll and L. E. Kavraki, "Path planning for deformable linear objects," *IEEE Transactions on Robotics*, vol. 22, no. 4, p. 625–636, 2006.

- [15] T. Bretl and Z. McCarthy, "Quasi-static manipulation of a kirchhoff elastic rod based on geometric analysis of equilibrium configurations," *The Int. J. of Robotics Research*, vol. 33, no. 1, pp. 48–68, 2014.
- [16] A. Sintov, S. Macenski, A. Borum, and T. Bretl, "Motion planning for dual-arm manipulation of elastic rods," *IEEE Robotics and Automation Letters*, vol. 5, no. 4, pp. 6065–6072, 2020.
- [17] A. S. I. Mishani, "Real-time non-visual shape estimation and robotic dual-arm manipulation control of an elastic wire," *IEEE Robotics and Automation Letters*, vol. 7, no. 1, pp. 422–429, 2021.
- [18] M. Yu, K. Lv, C. Wang, M. Tomizuka, and X. Li, "A coarse-to-fine framework for dual-arm manipulation of deformable linear objects with whole-body obstacle avoidance," in *ICRA*, 2023, pp. 10 153–10 159.
- [19] C. Wang, Y. Zhang, X. Zhang, Z. Wu, X. Zhu, S. Jin, T. Tang, and M. Tomizuka, "Offline-online learning of deformation model for cable manipulation with graph neural networks," *IEEE Robotics and Automation Letters*, vol. 7, no. 2, pp. 5544–5551, 2022.
- [20] D. Navarro-Alarcon, H. M. Yip, Z. Wang, Y. Liu, F. Zhong, T. Zhang, and P. Li, "Automatic 3-d manipulation of soft objects by robotic arms with an adaptive deformation model," *IEEE Transactions on Robotics*, vol. 32, no. 2, pp. 429–441, 2016.
- [21] R. Lagneau, A. Krupa, and M. Marchal, "Automatic shape control of deformable wires based on model-free visual servoing," *IEEE Robotics and Automation Letters*, vol. 5, no. 4, pp. 5252 – 5259, 2020.
- [22] S. Levvyakov and V. V. Kuznetsov, "Stability analysis of planar equilibrium configurations of elastic rods subjected to end loads," *Acta Mech*, vol. 211, p. 73–87, 2010.
- [23] F. Gu, Y. Zhou, Z. Wang, S. Jiang, and B. He, "A survey on robotic manipulation of deformable objects: Recent advances, open challenges and new frontiers," *arXiv:2312.10419*, 2023.
- [24] M. S. R. Varghese, "Yolov8: A novel object detection algorithm with enhanced performance and robustness," *International Conference on Advances in Data Engineering and Intelligent Computing Systems*, 2024.
- [25] K. He, X. Zhang, and J. S. Shaoqing Ren, "Deep residual learning for image recognition," *arXiv:1512.03385v1*, 2015.
- [26] R. F. Hartl, S. P. Sethi, and R. G. Vickson, "A survey of the maximum principles for optimal control problems with state constraints," *SIAM Review*, vol. 37, no. 2, pp. 181–218, 1995.
- [27] J. Z. Ben-Asher, *Optimal Control Theory with Aerospace Applications*. Reston, Virginia: AIAA Inc., 2010.
- [28] L. S. Pontryagin, V. G. Boltyanskii, R. V. Gamkrelidze, and E. F. Mishchenko, *The Mathematical Theory of Optimal Processes*. Interscience Publishers John Wiley & Sons, New York-London, 1962.
- [29] A. Love, *The Mathematical Theory of Elasticity*. Dover, New York, 1944.
- [30] J.-R. Sack and J. Urrutia, *Handbook of Computational Geometry*. Carleton University, 2000.
- [31] P. J. Huber, "Robust estimation of a location parameter," *Ann. Math. Statist*, vol. 35, no. 1, pp. 73–101, 1964.
- [32] I. Grinberg and A. Levin, "DLO Placement scheme Git," Mechanical Engineering, Technion, <https://github.com/ItayGrinberg93/Deformable-Linear-Object-Surface-Placement-Using-Elastica-Planning-and-Local-Shape-Control.git>, GitHub: <https://github.com/ItayGrinberg93/Deformable-Linear-Object-Surface-Placement-Using-Elastica-Planning-and-Local-Shape-Control.git>, 2025.